Available online at www.sciencedirect.com
ScienceDirect
Polymer 48 (2007) 2919–2927
polymer
www.elsevier.com/locate/polymer

Dynamic interplay between phase separation and crystallization in a poly(ε-caprolactone)/poly(ethylene glycol) oligomer blend

Wei-Tsung Chuang [a,b], U.-Ser. Jeng [b], Po-Da Hong [a,*], Hwo-Shuenn Sheu [b], Ying-Huang Lai [b], Kan-Shan Shih [c]

[a] *Department of Polymer Engineering, National Taiwan University of Science and Technology, Taipei 106, Taiwan*
[b] *National Synchrotron Radiation Research Center, Hsinchu 300, Taiwan*
[c] *School of Dentistry, National Defense Medical Center, Taipei 114, Taiwan*

Received 14 January 2007; received in revised form 3 March 2007; accepted 7 March 2007
Available online 18 March 2007

Abstract

We have investigated the crystallization effect on the phase separation of a poly(ε-caprolactone) and poly(ethylene glycol) oligomer (PCL/PEGo) blending system using simultaneous small-angle light scattering and differential scanning calorimetry (SALS/DSC) as well as simultaneous small-angle X-ray scattering (SAXS), wide-angle X-ray scattering (WAXS), and DSC (SAXS/WAXS/DSC). When the PCL/PEGo system, of a weight ratio of 7/3, is quenched from a melt state (160 °C) to temperatures below the spinodal point and the melting temperature of PCL (63 °C), the structural evolution observed exhibits characteristics of (I) early stage of spinodal decomposition (SD), (II) transient pinning, (III) crystallization-induced depinning, and (IV) diffusion-limited crystallization. The time-dependent scattering data of SALS, SAXS and WAXS, covering a wide range of length scale, clearly show that the crystallization of PCL intervenes significantly in the ongoing viscoelastic phase separation of the system, only after the early stage of SD. The effect of preordering before crystallization revives the structural evolution pinned by the viscoelastic phase separation. The growth of SAXS intensity during the preordering period conforms to the Cahn–Hilliard theory. In the later stage of the phase separation, the PCL-rich matrix, of spherulite crystalline domains developed due to the faster crystallization kinetics, traps the isolated PEGo-rich domains of a slower viscoelastic separation.

Keywords: Crystallization; Viscoelastic phase separation; Spinodal decomposition

1. Introduction

For a polymer blend system containing semicrystalline and amorphous components, the system morphology quenched from melt can be kinetically trapped through quench temperature and quench process, which modulate the competition/cooperation between the phase separation and crystallization of the system. For instance, when the melt of a binary polymer blend, of partly miscible or immiscible components, is quenched to a temperature below the spinodal temperature but above the melting temperature of the crystalline component, the morphology of the binary polymer blend is mainly determined by the phase separation kinetics [1–6]. Numerous studies have established a spinodal decomposition (SD) model for characterizing the phase separation behavior, including the exponential growth of light scattering intensity with time [7] in the early stage of the spinodal decomposition and the self-similarly growth [8] in the later stage. Recently, many interesting morphologies such as network-like and sponge-like as well as the unusual phase separation behavior like spinodal pinning and phase inversion, have been observed in various polymer blend systems [9,10]. These phenomena were attributed to the effects of viscoelastic liquid–liquid phase separation (LLPS) originated from an asymmetrically molecular dynamics (relating to, e.g., mobility of the molecules) existing between the two blend components [9–16].

* Corresponding author. Tel.: +886 2 27376539; fax: +886 2 27376544.
E-mail address: poda@mail.ntust.edu.tw (P.-D. Hong).

0032-3861/$ - see front matter © 2007 Elsevier Ltd. All rights reserved.
doi:10.1016/j.polymer.2007.03.041

When the temperature is quenched below both the spinodal point and the melting temperature of the crystalline component of the binary blend, the final morphology and structural properties of the system are compounded by the additional crystallization effect coexisting with the liquid–liquid phase separation. With the intervening of the crystallization effect, the transit pinning of the viscoelastic phase separation can be depinned, through local density fluctuations. The local density fluctuations induce a preordering process prior to crystallization, as reported in many studies [17–23]. For instance, Imai et al. [17,18] and Balta-Calleja et al. [19] monitored the growth of a SAXS peak during the induction period of polymer crystallization, and explained the observed growth behavior with the spinodal mechanism given by the Cahn–Hilliard theory [7]. Ryan et al. [20–22] also observed similar preordering effects in the melt-crystallized isotactic polypropylene using simultaneous SAXS/WAXS/DSC measurements. In addition, the pre-crystallization behavior was explained in detail by Olmsted et al. [23], through spinodal-type kinetics, on the basis of the Cahn–Hilliard theory [7].

The interplay between the phase separation and crystallization provides a possibility to tailor the final morphology of a polymer blend for specific applications via a control of the kinetic process of the LLPS and crystallization, for (1) simultaneous phase separation and crystallization, (2) phase separation-induced crystallization, or (3) crystallization-induced phase separation. Along this direction, a large number of studies have been made [24–33]. For instance, Hashimoto et al. [28,29] found that the structural evolution of the phase separation could be frozen by the rapid crystallization in the isotactic polypropylene (iPP)/ethylene–propylene random copolymer (EPR) mixtures. In the study of poly(ethylene-*co*-hexene) (PEH)/poly(ethylene-*co*-butene) (PEB), Han et al. [30] proposed that the growth of concentration fluctuations for interdiffusion during the LLPS could assist the orienting of the chain segments of PEB in forming nuclei for crystallization.

While the studies mentioned above focused on the result of the interplay between phase separation and crystallization, here we are interested more in capturing/manipulating the interaction or cooperation process of the two forces in a polymer blend, as well as the intermediate structures that can possibly be trapped. To study the structural evolution of a binary polymer blend system involving phase separation of a scale from nanometer to micron size, small-angle light scattering (SALS) and synchrotron small-angle X-ray scattering (SAXS) of a high X-ray flux are appropriate tools, whereas synchrotron wide-angle X-ray scattering is an ideal probe for the crystallization process in a time scale of seconds. Furthermore, to correlate the effects of phase separation to crystallization, simultaneous measurements of SALS/DSC and SAXS/WAXS/DSC can offer significant advantages over separate experiments.

In this study, we have specifically chosen a binary system of PCL/PEGo blend (7/3 weight ratio), with a pronounced viscoelastic phase separation and a good crystallization capability (PCL). As a consequence, the structural evolution influenced by the concomitant liquid–liquid phase separation and crystallization proceeds in a reasonable speed that allows us to capture the details of phase separation and crystallization using simultaneous SALS/DSC (for morphology changes in a large scale of micron size) and simultaneous SAXS/WAXS/DSC (for morphology changes in nano-to-meso scale and crystalline structure), when the system jumped from a melt to a temperature below the spinodal point and the melting temperature of PCL.

2. Experimental method

2.1. Sample preparation

Poly(ε-caprolactone) (PCL) and poly(ethylene glycol) oligomer (PEGo), with weight-averaged molecular weights (M_w) 10 000 and 400 Da, respectively, were received from Aldrich Chem. Co., and molten-mixed with a weight ratio of 7/3 (PCL/PEGo) at 160 °C. The blend sample was kept at 160 °C for 10 min on a hot stage and then transferred (within a few seconds) into a DSC chamber for phase separation and crystallization at 40 °C, 42 °C, 45 °C, and 48 °C, and for solely phase separation at 65 °C. The DSC instrument (Mettler-Toledo FP84), calibrated by the two commonly used standard samples of indium and zinc, was equipped with glass or Kapton windows, for either simultaneous SALS/DSC or SAXS/WAXS/DSC measurements, as detailed below.

2.2. Small-angle light scattering

The He–Ne laser, of a power 5 mW, used in our simultaneous SALS/DSC measurements was plane-polarized, with a selectable polarization direction. Light scattering pattern from the sample sealed inside the DSC cell with glass windows was collected by a CCD detector (with a time resolution of a second), equipped with a polarization analyzer. With the beam polarizer and analyzer in the same direction of polarization (V_v mode), the detector collected mainly the isotropic scattering contributed by the spinodal concentration fluctuations; with orthogonal polarizations (H_v mode), the detector collected only anisotropic scattering from the crystalline domains. The details of the SALS setup were reported in our previous work [34]. All the SALS data were corrected for background intensity. For the V_v mode, the one-dimensional scattering curves $I(q)$ were circularly averaged from the isotropic, two-dimensional scattering patterns measured. Whereas for the H_v mode, $I(q)$ profiles were obtained along the two symmetrical scattering axes of the two-dimensional scattering patterns (shown below), using a program specially developed for the instrument.

2.3. SAXS and WAXS measurements

Simultaneous SAXS/WAXS/DSC measurements were performed with X-rays of a wavelength of $\lambda = 1.91$ Å (6.5 keV) on the SWAXS instrument at the BL17B3 SWAXS endstation of the National Synchrotron Radiation Research Center

(NSRRC), Taiwan. With an area detector for SAXS and a linear detector for WAXS (both are gas proportional detectors), time-dependent SAXS/WAXS data were collected for the sample sealed inside the DSC chamber, with a data collection time of 60 s for each time frame. The sample-to-detector distance was 2772 mm for SAXS and 62 mm for WAXS. The setup covered q-ranges of 0.025–1.8 nm^{-1} in SAXS and 11–22 nm^{-1} in WAXS. All the SAXS and WAXS data were rigorously corrected for electronic noise, sample transmission, background scattering, and detector sensitivity, and calibrated by polyethylene and silver behenate for SAXS and by silicon and sodalite for WAXS. The one-dimensional SAXS intensity profiles $I(q)$ were circularly averaged from the two-dimensional isotropic scattering patterns. The details for SWAXS instrument were reported previously [35].

3. Data analysis

3.1. Lamellar model for SAXS data analysis

In semicrystalline polymer systems, lamellar structure of crystalline–amorphous type is often characterized by one-dimensional correlation function [36],

$$\gamma(x) = \frac{1}{Q}\int_0^\infty I(q)q^2\cos(qx)\mathrm{d}q, \quad (1)$$

obtained from the Fourier transform of the corresponding one-dimensional SAXS intensity profile, $I(q)$, with the scattering invariant Q and the scattering wavevector transfer $q = 4\pi \sin\theta/\lambda$ defined by the scattering angle 2θ and the wavelength λ of photons. Limited by the measurable q-range, it is often needed to extrapolate SAXS data in both high-q and low-q regions using, respectively, the Porod–Ruland [37] model and the Debye–Bueche model [38,39] before the Fourier transformation of $I(q)$ for $\gamma(x)$. Nevertheless, in this study a relative invariant Q_{SAXS} $(=\int_{q_1}^{q_2} Iq^2\mathrm{d}q)$ was used with the two integration limits approximated by the two measurable minimum and maximum q values, q_1 and q_2. In our case, the relative invariant thus obtained is found to be within few percent difference from the Q invariant obtained with the data extrapolation method. Fig. 1a illustrates a typical $\gamma(x)$ obtained from the SAXS profile measured for the system studied. From $\gamma(x)$, we can extract the amorphous thickness, crystalline thickness, and long period for the lamellar structure of PCL, as indicated in the figure.

3.2. Relative crystallinity extracted from WAXS

The relatively crystallinity $W_{C,WAXS}$ in this study is defined as the ratio of the integrated intensity of all Bragg peaks observed to the integrated intensity of the whole WAXS profile of the polymer blend studied. We fit the crystalline peak positions and integrated peak intensities with a Gaussian function, using a common peak-fitting program. The uncertainties of the fitted parameters are generally smaller than few percent.

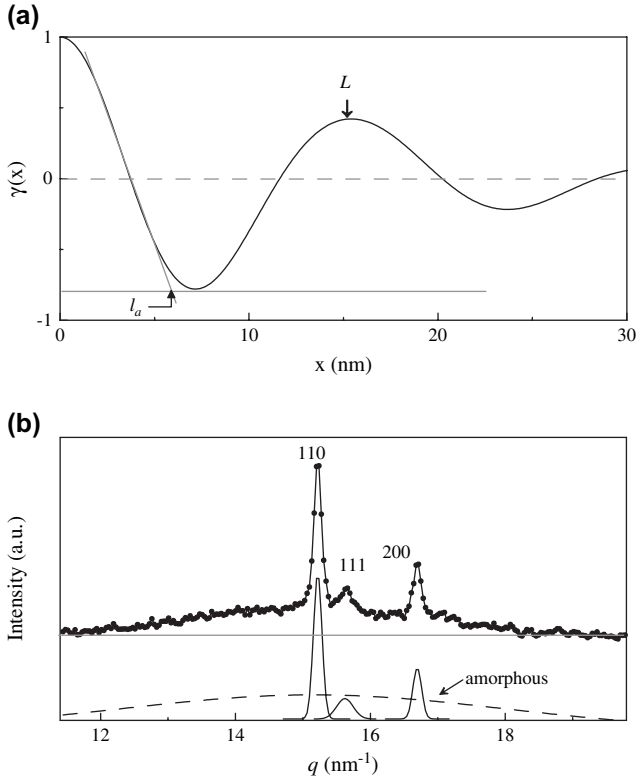

Fig. 1. (a) A typical $\gamma(x)$ obtained from a SAXS profile measured for the PCL/PEGo (7/3) system, with the amorphous thickness l_a and the long period L of the lamellar structure of PCL indicated. (b) Typical WAXS data obtained at $T_c = 45\,^\circ C$ for the PCL/PEGo blend during crystallization. The data are deconvoluted into three Gaussian peaks for the 110, 111, 200 Bragg reflections and a broad amorphous halo.

Fig. 1b demonstrates a typical case, where the WAXS data are deconvoluted by three crystalline peaks and an amorphous halo.

4. Experimental results

Fig. 2 shows the phase diagram determined previously [40] for the PCL/PEGo blend of an upper critical solution temperature (UCST). With the sample composition of 7/3 and the initial sample temperature of 160 °C, five quenched temperatures, 65 °C, 48 °C, 45 °C, 42 °C, and 40 °C, are selected (marked in Fig. 2). The designated route of phase separation (indicated in Fig. 2) crosses over the spinodal and melting curves from the one-phase region and enters into the zone where crystallization coexists with liquid–liquid phase separation.

4.1. SALS/DSC data

Fig. 3 shows the time-dependent SALS patterns collected with the V_v and H_v modes defined previously, after the sample quenched from 160 °C to 45 °C for an isothermal phase separation and crystallization. Within the first 16 s after the quench, the isotropic spinodal ring appears in the V_v mode while little or no scattering intensity can be observed in the H_v mode (Fig. 3a). At $t = 340$ s after quench (Fig. 3b), very

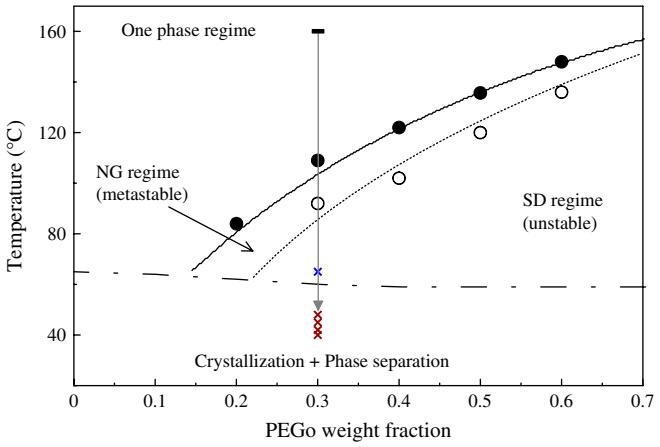

Fig. 2. Phase diagram of the PCL/PEGo blend. The solid and empty circles are obtained from light scattering measurements for the PCL/PEGo blend, with the solid and dotted curves drawn for the binodal and spinodal curves. NG and SD denote, respectively, nucleation-and-growth and spinodal decomposition. Below the melting line (dashed line) is the coexisting phase of crystallization and liquid–liquid phase separation. The arrow indicates the route of phase separation selected in this study, from 160 °C to 65 °C, 48 °C, 45 °C, 42 °C, and 40 °C (marked by the crosses), respectively.

low angle scattering near the beam center appears in the V_v mode, with an enhanced spinodal ring. Whereas in the H_v mode, a cross pattern of anisotropic scattering starts to show up vaguely. This weak scattering, occurring with no exothermic sign in the DSC trace, corresponds to large-scale anisotropic fluctuations in the system, instead of PCL crystallization. In the subsequent evolution after 340 s (Fig. 3c–e), the scattering near the beam center in the V_v mode develops into an elliptic-like pattern. Meanwhile, the anisotropic scattering in the H_v mode intensifies, accompanied with the prominent exothermic peak of the PCL crystallization, and forms the four-leaf-clover pattern in the lower-q region. The evolution of the scattering pattern observed reflects the typical morphological development of polymer crystals from sheaf-like crystal to spherulites.

Fig. 4 exhibits the one-dimensional scattering profiles obtained from the scattering patterns shown in Fig. 3. For isotropic scattering, the scattering profiles (Fig. 4a) are characterized by the spinodal scattering hump centered at q_{m,V_v}, with the peak intensity I_{m,V_v}. The characteristic peak position $q_{m,V_v} \sim 1.2\ \mu m^{-1}$ indicates a mean spacing of 5.2 μm ($\Lambda = 2\pi/q_{m,V_v}$) between the phase separated domains. The time-dependent q_{m,H_v} and I_{m,V_v} values obtained from the scattering profiles are summarized in Fig. 5. On the other hand, the scattering profiles retrieved from the anisotropic scattering patterns (contributed mainly by the PCL spherulites) gradually develop a scattering peak at $q_{m,H_v} = 0.21\ \mu m^{-1}$ at $t \sim 720$ s, in which peak position corresponds to an averaged size D ($=4.1/q_{m,H_v}$) [41], ca. 20 μm of the PCL spherulites. The size is evidently larger than the domain spacing Λ (ca. 5 μm) of the phase separated domains, indicating the formation of PCL matrix in the system. Note, to better determine the timing of the appearance of the anisotropic scattering, it is important to eliminate completely the isotropic scattering

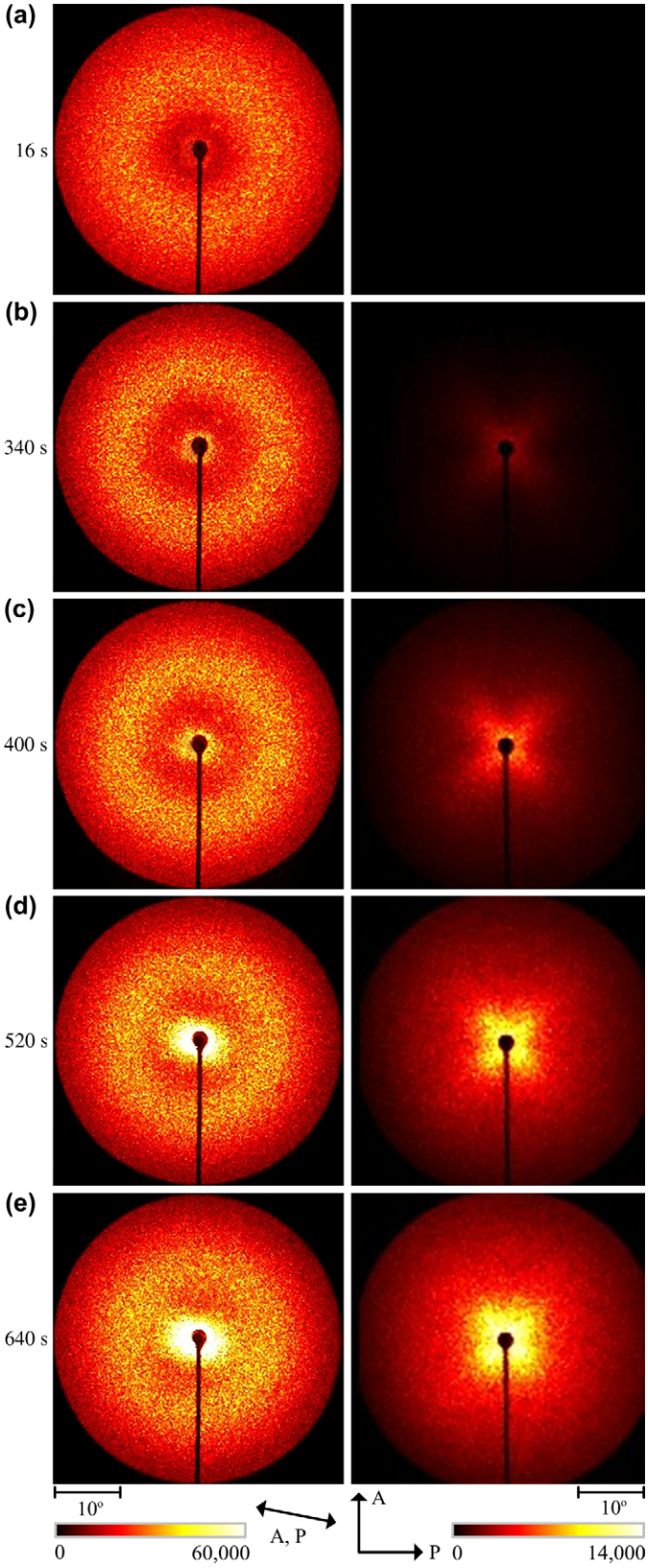

Fig. 3. Time-dependent SALS patterns measured in the V_v mode (left) and H_v mode (right) for the PCL/PEGo (7/3) blend quenched from 160 °C to 45 °C. At the bottom, A and P denotes the directions of polarizer and analyzer.

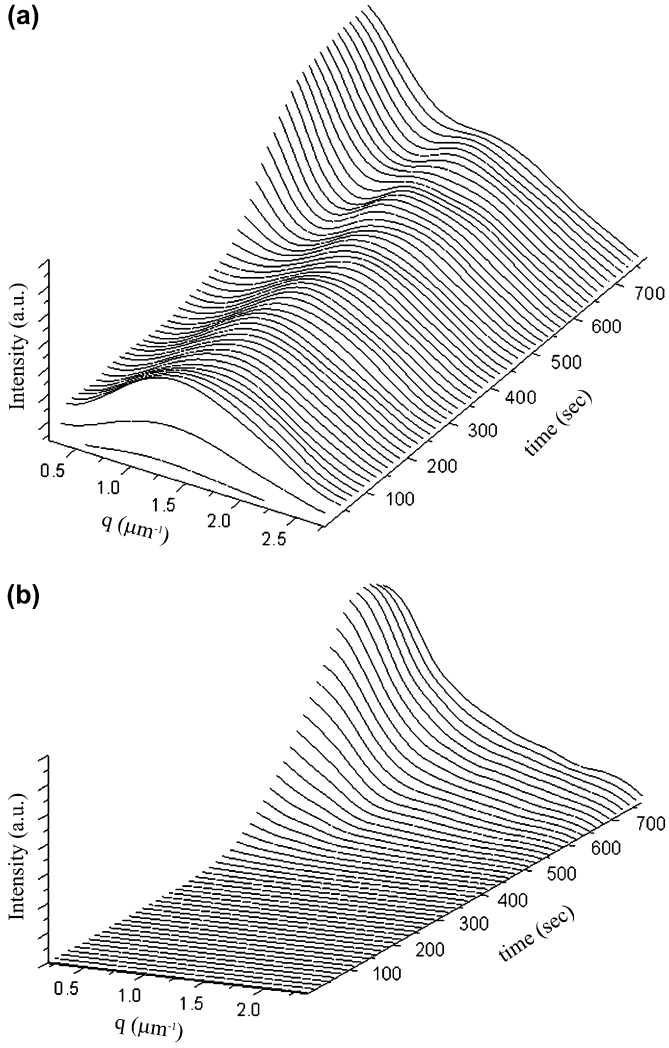

Fig. 4. Time-resolved scattering profiles extracted from the two-dimensional scattering patterns shown in Fig. 3, with (a) isotropic scattering (V_v mode) and (b) anisotropic scattering (H_v mode).

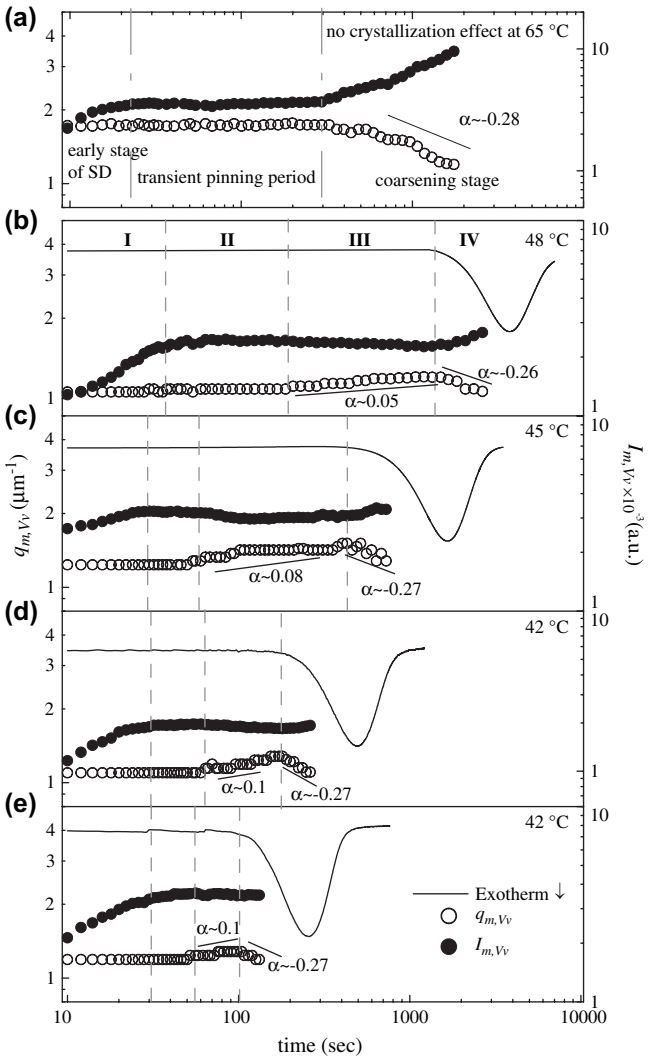

Fig. 5. Time-dependent q_{m,V_v} (plotted with the left-hand-side scale) and I_{m,V_v} (plotted with the right-hand-side scale) extracted from the SALS data taken after the polymer blend PCL/PEGo is quenched from 160 °C to (a) 65 °C, (b) 48 °C, (c) 45 °C, (d) 42 °C, and (e) 40 °C, respectively. Also shown are the simultaneously measured DSC traces (solid curves). The dotted lines split the phase separation process into four distinct time zones, I, II, III, and IV, as labeled in (b) for example. The α values are extracted from the slopes of the corresponding short solid lines.

contribution from the spinodal ring in the H_v mode data collection. For this purpose, the orthogonal alignment between the polarizer and analyzer needs to be accurate within 1°.

In Fig. 5, we summarize the series of SALS data observed for the sample quenched from 160 °C to the temperature above and below the melting temperature of PCL, $T_m = 63$ °C. According to the features of the spinodal peak position and peak intensity, q_{m,V_v} and I_{m,V_v}, we divide phase separation into four characteristic stages as indicated in Fig. 5b–e. In Stage I, I_{m,V_v} grows exponentially with a constant q_{m,V_v} (namely, phase separation increases continuously with a constant domain spacing), which corresponds well to the early stage of SD and there is little or no observable crystallization effect. In Stage II, the constants q_{m,V_v} and I_{m,V_v} correspond to a transient pinning stage of phase separation. From Fig. 5a (data of no crystallization effect) and Fig. 5d,e (data of increasingly larger crystallization effect due to the deeper quench), we notice the effect of lower quench temperature on shortening the duration of the pinning stage for an earlier entry into the subsequent Stage III. In Stage III, the unusual increase in q_{m,V_v}, few percent (~3–5%) at most, is a unique crystallization-induced effect, as compared to the process of solely liquid–liquid phase separation of a monotonic decrease in the q_{m,V_v} value (see Fig. 5a). For this effect, we assign this Stage III as crystallization-induced depinning region. From the four sets of data in Fig. 5b–e, obviously, the duration of this stage can be reduced more by a deeper quench of the system into a lower temperature for a larger crystallization effect. The increase of the q_{m,V_v} value can be characterized by a power-law behavior $q_{m,V_v} \sim t^{\alpha}$, with positive α values ranging from 0.05 (Fig. 5b) to 0.1 (Fig. 5e). The negative α value corresponds to a faster transition to the Stage IV for crystallization. In Stage IV, the decreasing q_{m,V_v} and increasing I_{m,V_v} with

time characterize the stage with a coarsening in the phase separated domains and an enhanced PCL crystallization, as evidenced by the prominent exothermic peak detected concurrently (solid curves in Fig. 5).

4.2. SAXS/WAXS/DSC data

Fig. 6 shows the time-resolved SAXS and WAXS data of the PCL/PEGo (7/3) blend during an isothermal crystallization at 45 °C. The WAXS profiles (Fig. 6a) measured show only an amorphous halo scattering in the earlier stage, until the first appearance of discernible crystalline peaks at $t \sim 600$ s. The three crystalline peaks observed are assigned to be the crystallographic reflections of the planes indexed by (110), (111), and (200) of the orthorhombic unit cell of PCL crystals [42]. Using the method described in the previous section, we have extracted the evolution of the relative crystallinity $W_{C,WAXS}$ from the time-dependent WAXS profiles.

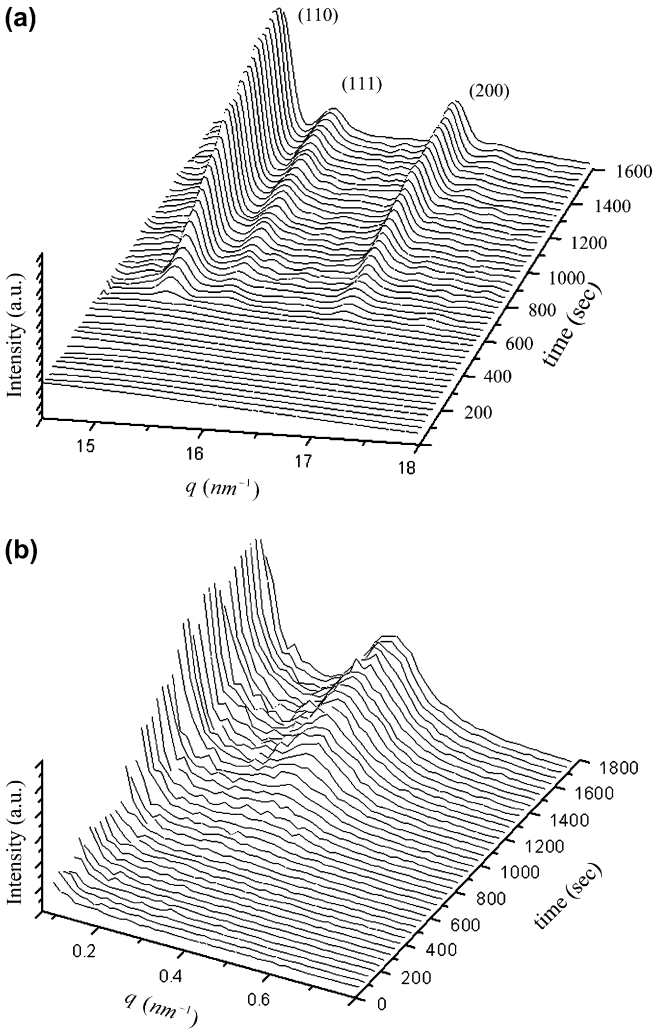

Fig. 6. Simultaneously measured (a) WAXS profiles and (b) the corresponding one-dimensional SAXS profiles, after the PCL/PEGo (7/3) blend quenched from 160 °C to 45 °C.

On the other hand, the corresponding SAXS profiles derived from the isotropic two-dimensional scattering patterns in the early stage of SD (Stage I) and the structural pinning stage (Stage II) are featureless, implying the lack of density fluctuations in nano-to-meso scale, despite the concentration fluctuations of micron size observed in the SALS (see Fig. 5). Around $t \sim 400$ s after the quench (in Stage III), the system gives discernible SAXS intensities in the low-q region (~ 0.1 nm^{-1}). When the first WAXS crystalline peaks appear, a broad SAXS halo takes shape at the same time. The halo gradually develops into a relatively sharp hump, signifying the formation of the PCL lamellar stacks.

The time-dependent SAXS profiles reveal a shift in the scattering peak position of the PCL lamellar stacks from $q = 0.32$ nm^{-1} to a larger $q \sim 0.37$ nm^{-1} (a sign of condensing lamellar spacing), as the lamellar structure develops along time. The detailed structural parameters of the lamellar stacks, including the long period L, crystalline thickness l_c, and the amorphous thickness l_a, are extracted from the one-dimensional correlation function $\gamma(x)$ Fourier transformed from the measured SAXS profiles, as described previously. To be consistent with the bulk crystallinity ~ 0.47 determined from the DSC result simultaneously measured, we assign the first minimum in the correlation function to be amorphous thickness l_a, based on the method described in our previous report [43]. The lamellar thickness then can be deduced from $l_c = L - l_a$. The lamellar thickness of PCL ($l_c = 8$–9 nm) measured is consistent with the value ~ 8 nm reported by Nojima et al. [33]. The time-dependent L, l_c, and l_a obtained from the SAXS profiles are summarized in Fig. 7.

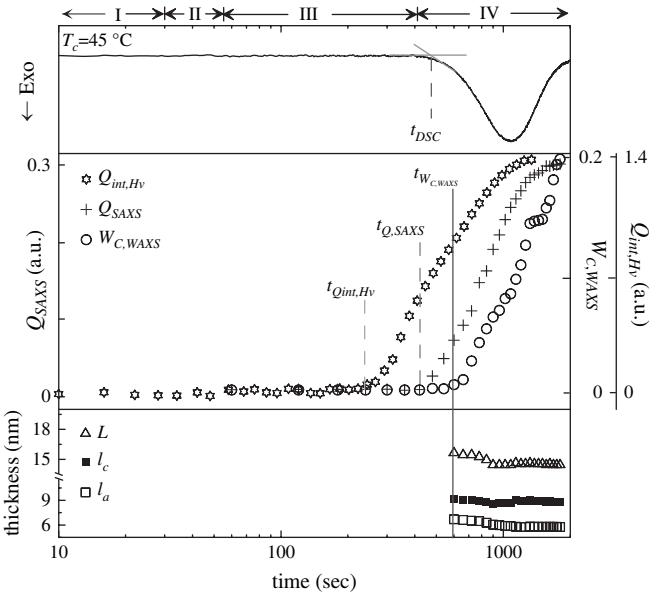

Fig. 7. The time evolutions of the measured structural parameters that characterize the phase separation of the PCL/PEGo system at 45 °C, including the exothermic trace from DSC (top); scattering invariant Q_{int,V_v} from SALS, relative invariant Q_{SAXS}, and relative crystallinity $W_{C,WAXS}$ (middle); long period L, crystalline thickness l_c, and amorphous thickness l_a from SAXS (bottom). The four characteristic times, t_{Q_{int},H_v}, $t_{Q,SAXS}$, t_{DSC} and $t_{W_{C,WAXS}}$ mark the initial changes of the corresponding quantities.

4.3. Global view of the scattering data

To correlate all the SALS, SAXS, WAXS, and DSC data for a comprehensive picture of the structural evolution of the blending system studied, we have integrated all the evolutions of the structural parameters observed in Fig. 7, according to the four structural evolution stages proposed previously. In Fig. 7, the structural evolution displayed covers a time scale ranging from 10 s to 2000 s and length scale from atomic to nano, meso, and micron size. For instance, the large domain spacing ~5 μm is first observed by SALS in Stages I and II, then density fluctuations of a meso-to-nano scale is picked by SALS or SAXS sometime later in Stage III. Afterwards, SAXS and WAXS detect the nano-scale ordering and the atomic ordering of the lamellar structure of PCL in Stage IV.

For the crystallization-involved structural transition (mainly in Stages III and IV), we have further defined four characteristic times $t_{Q_{\mathrm{int}},\mathrm{H_v}}$, $t_{\mathrm{Q,SAXS}}$, t_{DSC}, and $t_{W_{\mathrm{C,WAXS}}}$ for the initiation of the changes in the $\mathrm{H_v}$ scattering invariant $Q_{\mathrm{int},\mathrm{H_v}}$ (SALS), relative invariant Q_{SAXS} (SAXS), exothermic heat flow (DSC), and relative crystallinity $W_{\mathrm{C,WAXS}}$ (WAXS). The time sequence $t_{Q_{\mathrm{int}},\mathrm{H_v}} < t_{\mathrm{Q,SAXS}} < t_{\mathrm{DSC}} < t_{W_{\mathrm{C,WAXS}}}$ illustrates the sequential changes of the system morphology before and during the PCL crystallization, with a focus on the transition from the later stage of Stage III to Stage IV. During the transition period near $t_{\mathrm{Q,SAXS}}$, the crystallization-induced local density fluctuations (of a nano-to-meso scale) start to affect the liquid–liquid phase separation process, and revive gradually the structure pinned by the viscoelastic effect of the system. The transition can be accelerated for an earlier domain coarsening and PCL crystallization (starting from $t_{W_{\mathrm{C,WAXS}}}$ in Stage IV), by quenching the system to a lower temperature below the melting temperature of PCL (see Fig. 5).

5. Discussion

5.1. Gibbs free energy of mixing compounded by crystallization

In this section, we describe how the free energy ΔG of mixing of the binary polymer system is affected by the crystallization, and how the resultant driving forces guide the phase separation process of the PCL/PEGo blend. Fig. 8 illustrates the two kinds of free energy landscapes for (1) T_{ps}, temperatures below spinodal temperature T_{s} but above the melting temperature T_{m} of PCL and (2) T_{c}, temperatures below T_{m} of PCL. When temperature of the binary system of PCL/PEGo (7/3) (corresponding to the PCL volume fraction $\phi_{\mathrm{PCL}} = 0.696$) is quenched from one-phase temperature to T_{ps}, the system undergoes a phase separation for the liquid–liquid binodal compositions, $\phi_{\mathrm{l}'}(T_{\mathrm{ps}})$ and $\phi_{\mathrm{l}''}(T_{\mathrm{ps}})$, of a local free energy minimum, following the SD process. On the other hand, when the temperature is quenched below T_{m}, both the two driving forces (derived from $\mathrm{d}(\Delta G)/\mathrm{d}\phi$)—the force of liquid–liquid phase separation (determined by the tangent line of two metastable liquid–liquid binodal points $\phi_{\mathrm{l}'}(T_{\mathrm{c}})$ and $\phi_{\mathrm{l}''}(T_{\mathrm{c}})$) and the force of crystallization (determined by the two stable liquid–solid phase compositions, $\phi_{\mathrm{L}}(T_{\mathrm{c}})$ and $\phi_{\mathrm{C}}(T_{\mathrm{c}})$)—can affect the route of the phase separation (see Fig. 8).

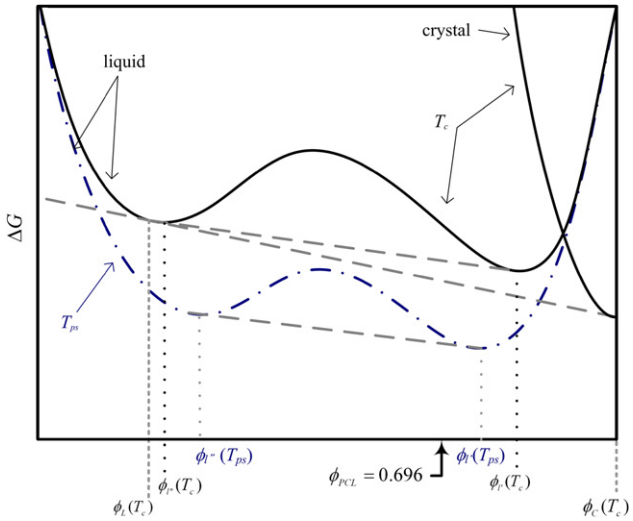

Fig. 8. Free energy landscapes of mixing of the binary polymer system at T_{ps} (dash-dotted curve; below spinodal temperature T_{s} but above the melting temperature T_{m} of PCL) and T_{c} (solid curve; below T_{m}). The arrow indicates the initial PCL volume fraction $\phi = 0.696$ for the PCL/PEGo (7/3) system studied. $\phi_{\mathrm{l}'}(T_{\mathrm{c}})$ and $\phi_{\mathrm{l}''}(T_{\mathrm{c}})$ are the two metastable liquid–liquid binodal points, whereas $\phi_{\mathrm{L}}(T_{\mathrm{c}})$ and $\phi_{\mathrm{C}}(T_{\mathrm{c}})$ are the stable liquid–solid phase compositions. The contribution of PCL crystallization to ΔG is also shown.

In this studied system, we have observed the development of SD before PCL crystallization (in Stage I), the pinning and depinning of the phase separation (in Stages II and III), and the crystallization (in Stage IV). The phase separation process observed follows well the free energy "map" given in Fig. 8 for the T_{c} case. It is possible to rearrange or tune the weighting of the two driving forces of the crystallization and liquid–liquid phase separation, through the selections of quenched temperature and initial composition, to trap the phase separation process in a local minimum of a selected ΔG landscape, thus, tailoring the final morphology through the kinetic competition between the two forces.

5.2. Interplay between phase separation and crystallization

With the guide of the free energy map shown above, we are now in a good position to discuss the cause and effect in the structural evolution of the system studied. With the phase separation features observed (see Figs. 5 and 7), we can see that Stage I for the early stage of SD is not affected by the crystallization. In Stage II, we attribute the transient pinning of the morphology mainly to the viscoelastic phase separation. For a dynamically asymmetric blend of PCL/PEGo, the PCL, of a much higher molecular weight and a lager viscoelastic effect, therefore, slower dynamics than PEGo, defers the progress of the phase separation. Transient pinning was also observed by Tanaka and Araki [9,10] in dynamically

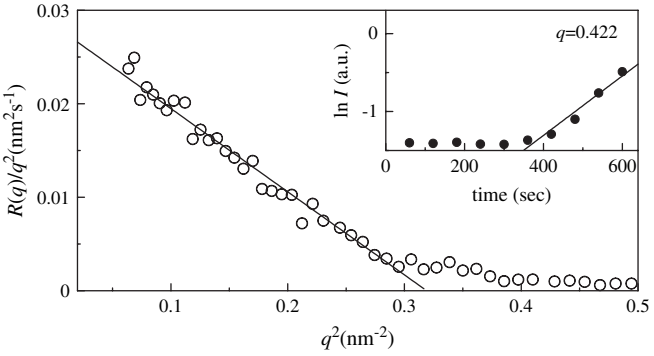

Fig. 9. $R(q)/q^2$ vs. q^2 plot for the growth rate $R(q)$ of the SAXS intensity $I(q)$ observed in the PCL preordering period of the PCL/PEGo (7/3) blend quenched to 45 °C. The data are fitted with a linear relation, with the interception at 0.028 nm^2 s^{-1} corresponding to the diffusion coefficient of the system. The inset shows a typical example of the exponential growth behavior of $I(q)$ with time, at $q = 0.422$ nm^{-1}. The data were fitted with the solid line for the linear relation of ln $I(q)$ vs. time.

asymmetric systems of polymer blends, who also explained the pinning effect by suppressed concentration fluctuations. However, in our case, with the intervening of a non-trivial crystallization force, the structural pinning effect can be overridden. Apparently, in our system the concentration fluctuations locked by the viscoelastic effect is gradually revived by the crystallization force for a preordering of PCL chains before crystallization.

In Stage III, characterized by the crystallization-induced structural depinning (see Fig. 5), we attribute the growing local density fluctuations with time (observed by SAXS) to a preordering of PCL segments. From the structural evolution sequence observed, the local density fluctuation or preordering of PCL closely correlates to the depinning process. The preordering overrides the viscoelastic-confined concentration fluctuations and leads to the decreased PCL domain spacing, as observed by the SALS. The decrease in the mean spacing of the PCL-rich domains (corresponding to the few percent increase in q_{m,V_v} shown in Fig. 5) may be a result of decreased PEGo domain volume (~10%), due to a crystallization-accelerated segregation of PCL from the PEGo-rich domains.

After t_{DSC} or $t_{W_{C,WAXS}}$ is Stage IV, defined as the diffusion-limited crystallization stage. In this stage, the formation of three-dimensional crystalline domains is concomitant with the formation of the lamellar domain of PCL (within a time resolution of a minute), indicating a close association between the three-dimensional packing and the lamellar stacking. Then, the lamellar domains maintain the size with the crystalline zones inside by growing into a matured structure (constant L, l_c, and l_a values). In the later stage of crystallization, the number of matured lamellar domains (Q_{SAXS}) and the relative crystallinity ($W_{C,WAXS}$) of the system increase with time. And the development of PCL crystalline morphology (from sheaf-like crystals to spherulites) inside the PCL-rich domains is faster than the coarsening process of the minor PEGo-rich domains (via the evaporation–condensation process). As a result, the PCL-rich domains develop into matrix of the system, with a characteristic size of spherulites larger than the mean domain spacing of the isolated PEGo domains. And the PCL matrix traps some of the isolated PEGo-rich domains of an incomplete phase separation, as evidenced by our observation using polarized microscope [43]. The result complies with the law – the fastest wins – in determining the kinetically trapped morphology, as also mentioned by Hashimoto et al. in the studies of diffusion-limited crystallization [28,29].

In the transition from Stage III to Stage IV (Fig. 7), there is a clear interval between $t_{Q,SAXS}$ and $t_{W_{C,WAXS}}$, where the SAXS relative invariant Q_{SAXS} rises before the appearance of $W_{C,WAXS}$ of the crystalline scattering, namely, the preordering period. In this period, the local density fluctuations of

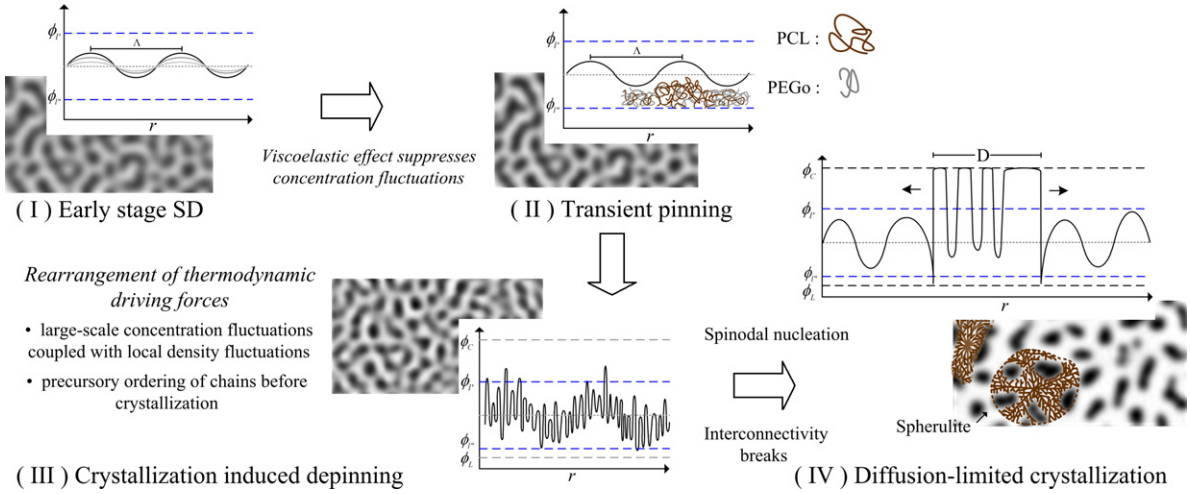

Fig. 10. Cartoons for the morphologies and the corresponding concentration (ϕ)/density fluctuations in the four stages, I, II, III, and IV, of the structural evolution of the PCL/PEGo (7/3) blend, with Λ for the wavelength of concentration fluctuations of the liquid–liquid phase separation and D for the size of PCL spherulites. The dark zones are for PEGo domains, whereas the relatively bright zones represent the PCL-rich domains of a higher viscoelasticity. The symbols for concentration ϕ are defined in Fig. 8.

preordering and the large-scale concentration fluctuations of liquid–liquid phase separation are superimposed, and the corresponding SAXS intensity observed follows reasonably well the exponential growth behavior $I(q,t) = I(q,t=0)\exp[2R(q)t]$ described by the Cahn–Hilliard theory [7], as the example (with $q = 0.422\ \mathrm{nm}^{-1}$) shown in the inset of Fig. 9. From the growth rate $R(q) = D_{\mathrm{app}}q^2(1 - (1/2)(q^2/q_{\mathrm{m}}(0)^2))$ of the SAXS intensity in the q-range of 0.25–0.55 nm^{-1}, we have extracted an apparent diffusion coefficient $D_{\mathrm{app}} = 0.028\ \mathrm{nm}^2/\mathrm{s}$ from the intercept, as shown in Fig. 9, with the most probable wavenumber of fluctuations $q_{\mathrm{m}}(0) = 0.40\ \mathrm{nm}^{-1}$ approximated by the long period L ($\sim 0.37\ \mathrm{nm}^{-1}$) observed. Nevertheless, the preordering behavior in SD is well studied by many groups, including, Imai et al. [17,18], Balta-Calleja et al. [19], Ryan et al. [20–22], and Olmsted et al. [23].

In Fig. 10, we graphically illustrate the interplay between the crystallization and phase separation described above, based on the evolution characteristics of the concentration/density fluctuations during the phase separation of the system. In Stage I, the long range concentration fluctuations of a characteristic length scale Λ ($\sim 5\ \mu\mathrm{m}$) correspond to the early stage of SD. In Stage II, the transient pinning, the amplitude of the long range density fluctuations enhances, while the fluctuation range Λ is confined by the viscoelastic effect. In Stage III, the crystallization-induced depinning, the local density fluctuations, corresponding to the preordering of PCL, superimpose the long range concentration fluctuations of liquid–liquid phase separation. We assume that the large local density fluctuations existing prior to the crystallization of PCL are responsible for the formation of stable PCL nuclei. In Stage IV, diffusion-limited crystallization, characteristic lamellar density fluctuations of the PCL spherulites keep expanding.

6. Conclusions

We have studied the phase separation of the PCL/PEGo (7/3) blend in a wide range of length scale and time scale, with the viscoelastic liquid–liquid phase separation compounded by the crystallization effect of PCL. After the early stage of SD of the system, the crystallization effect is initiated, and the structural evolution pinned by the viscoelastic effect is depinned by the crystallization force through local density fluctuations. The large PCL-rich domains of PCL spherulites further suppress the ongoing viscoelastic separation in the later stage of the phase separation. Since kinetic competing rule abides by the law – the fastest wins, we can control the competition between phase separation and crystallization by the initial composition and quenched temperature for a particular degree of phase separation of a preferred morphology.

Acknowledgment

The work was partially supported by the NSC under grant no. NSC-94-2216-E-011-001.

References

[1] de Gennes PG. J Chem Phys 1980;72:4756.
[2] Gunton JD, Miguel MS, Sahni P. In: Domb C, Lebowitz JL, editors. Phase transitions and critical phenomena, vol. 8. New York: Academic Press; 1983. p. 269–466.
[3] Binder K. Adv Polym Sci 1994;112:181.
[4] Bates FS, Wiltzius P. J Chem Phys 1989;91:3258.
[5] Hashimoto T, Itakura M, Shimidzu N. J Chem Phys 1986;85:6773.
[6] Hashimoto T. In: Cahn RW, Haasen P, Kramer EJ, editors. Materials science and technology, vol. 12. Weinheim: VCH; 1993. p. 252–300.
[7] Cahn JW, Hilliard JE. J Chem Phys 1958;28:258 and; J Chem Phys 1959;31:688.
[8] Furukawa H. Physica A 1984;123:497.
[9] Tanaka H. Phys Rev Lett 1993;71:3158; J Chem Phys 1994;100:5323 and; Phys Rev Lett 1996;76:787.
[10] Tanaka H, Araki T. Phys Rev Lett 1997;78:4966.
[11] Taniguchi T, Onuki A. Phys Rev Lett 1996;77:4910.
[12] Clarke N, McLeish TCB, Pavawongsak S, Higgins JS. Macromolecules 1997;30:4459.
[13] Cao Y, Zhang H, Xiong Z, Yang Y. Macromol Theory Simul 2001;10:314.
[14] Takenaka M, Takeno H, Hasegawa H, Saito S, Hashimoto T, Nagao M. Phys Rev E 2002;65:021806.
[15] Dwivedi V, Ahluwalia R, Lookman T, Saxena A. Phys Rev E 2004;70:011506.
[16] Luo K, Gronski W, Friedrich C. Eur Phys J E 2004;15:177.
[17] Imai M, Mori K, Mizukami T, Kaji K, Kanaya T. Polymer 1992;33:4451. and 1992;33:4457.
[18] Imai M, Kaji K, Kanaya T. Phys Rev Lett 1993;71:4162.
[19] Ezquerra TA, Lopez-Cabarcos E, Hsiao BS, Balta-Calleja FJ. Phys Rev E 1996;54:989.
[20] Terrill NJ, Fairclough PA, Towns-Andrews E, Komanschek BU, Young RJ, Ryan AJ. Polymer 1998;39:2381.
[21] Ryan AJ, Fairclough JPA, Terrill NJ, Olmsted PD, Poon WCK. Faraday Discuss 1999;112:13.
[22] Heeley EL, Maisens AV, Olmsted PD, Bras W, Dolbnya IP, Fairclough JPA, et al. Macromolecules 2003;36:3656.
[23] Olmsted PD, Poon WCK, McLeish TCB, Terrill NJ, Ryan AJ. Phys Rev Lett 1998;81:373.
[24] Tanaka H, Nishi T. Phys Rev Lett 1985;55:1102.
[25] Burghardt WR. Macromolecules 1989;22:2482.
[26] Chen HL, Hwang JC, Yang JM, Wang RC. Polymer 1998;39:6983.
[27] Shabana HM, Olley RH, Bassett DC, Jungnickel BJ. Polymer 2000;41:5513.
[28] Inaba N, Sato K, Suzuki S, Hashimoto T. Macromolecules 1986;19:1690.
[29] Inaba N, Yamada T, Suzuki S, Hashimoto T. Macromolecules 1988;21:407.
[30] Zhang X, Wang Z, Muthukumar M, Han CC. Macromol Rapid Commun 2005;26:1285.
[31] Wang H, Shimizu K, Kim H, Hobbie EK, Wang ZG, Han CC. J Chem Phys 2002;116:7331.
[32] Wang H, Shimizu K, Hobbie EK, Wang ZG, Meredith JC, Karim A, et al. Macromolecules 2002;35:1072.
[33] Nojima S, Satoh K, Ashida T. Macromolecules 1991;24:942.
[34] Chou CM, Hong PD. Macromolecules 2003;36:7331.
[35] Lai YJ, Sun YS, Jeng U, Lin JM, Lin TL, Sheu HS, et al. J Appl Crystallogr 2006;39:871.
[36] Strobl GR, Schneider M. J Polym Sci Part B Polym Phys 1980;18:1343.
[37] Ruland WJ. J Appl Crystallogr 1971;4:70.
[38] Debye P, Bueche AM. J Appl Phys 1949;20:518.
[39] Debye P, Anderson Jr HR, Brumberger H. J Appl Phys 1957;28:679.
[40] Chuang WT, Shih KS, Hong PD. J Polym Res 2005;12:197.
[41] Stein RS, Rhodes MB. J Appl Phys 1960;31:1873.
[42] Hu H, Dorset DL. Macromolecules 1990;23:4604.
[43] Chuang WT, Jeng US, Sheu HS, Hong PD. Macromol Res 2006;14:45.